Free- and reference-layer magnetization modes versus in-plane magnetic field in a magnetic tunnel junction with perpendicular magnetic easy axis

Hamid Mazraati,[1,2] Tuan Q. Le,[2] Ahmad A. Awad,[1,3] Sunjae Chung,[2,3] Eriko Hirayama,[4] Shoji Ikeda,[4,5,6] Fumihiro Matsukura,[4,5,7] Hideo Ohno,[4,5,6,7] and Johan Åkerman[1,2,3]

[1]*NanOsc AB, SE-Kista 164 40, Sweden*

[2]*Department of Materials and Nanophysics, School of Information and Communication Technology, KTH Royal Institute of Technology, Electrum 229, SE-16440 Kista, Sweden*

[3]*Department of Physics, University of Gothenburg, SE-412 96, Gothenburg, Sweden*

[4]*Laboratory for Nanoelectronics and Spintronics, Research Institute of Electrical Communication, Tohoku University, 2-1-1 Katahira, Aoba-ku, Sendai 980-8577, Japan*

[5]*Center for Spintronics Integrated Systems, Tohoku University, 2-1-1 Katahira, Aoba-ku, Sendai 980-8577, Japan*

[6]*Center for Innovative Integrated Electronic Systems, Tohoku University, 468-1 Aramaki Aza Aoba, Aoba-ku, Sendai 980-0845, Japan*

[7]*WPI Advanced Institute for Materials Research, Tohoku University, 2-1-1 Katahira, Aoba-ku, Sendai 980-8577, Japan*

(Received 8 April 2016; revised manuscript received 21 July 2016; published 26 September 2016)

We study the magnetodynamic modes of a magnetic tunnel junction with perpendicular magnetic easy axis (p-MTJ) in in-plane magnetic fields using device-level ferromagnetic resonance spectroscopy. We compare our experimental results to those of micromagnetic simulations of the entire p-MTJ. Using an iterative approach to determine the material parameters that best fit our experiment, we find excellent agreement between experiments and simulations in both the static magnetoresistance and magnetodynamics in the free and reference layers. From the micromagnetic simulations, we determine the spatial mode profiles, the localization of the modes and, as a consequence, their distribution in the frequency domain due to the inhomogeneous internal field distribution inside the p-MTJ under different applied field regimes. We also conclude that the excitation mechanism is a combination of the microwave voltage modulated perpendicular magnetic anisotropy, the microwave Oersted field, and the spin-transfer torque generated by the microwave current.

DOI: 10.1103/PhysRevB.94.104428

I. INTRODUCTION

Magnetic tunnel junctions (MTJs) with CoFeB free and reference layers and an MgO tunnel barrier are generating tremendous interest due to their attractive combination of a very high tunnel magnetoresistance (TMR) [1–4] and a magnetic anisotropy that can be varied from easy plane to perpendicular by changing the CoFeB thickness [5–9].

In order to understand and develop the functionality of MTJs with perpendicular magnetic easy axis (p-MTJs), it is necessary to understand both their static and dynamic magnetization properties as a function of the external magnetic field. In particular, both magnetization switching and steady magnetization precession rely on the available magnetodynamic modes, their field dependence, and their spatial profiles. For MTJs with an in-plane easy axis and magnetization saturated by a perpendicular magnetic field, this has already been characterized in great detail by Naletov *et al.* [10]. However, the reciprocal geometry of a pillar with strong perpendicular magnetic anisotropy (PMA) in both the free and reference layers in an in-plane magnetic field has to date often been dealt with in a macrospin approximation and in a limited field range, where it has been further assumed that only the free layer is significantly affected by the applied field [11–14].

In this study, we use magnetoresistance (MR) and so-called homodyne-detected ferromagnetic resonance (FMR) [15–17] to study the static and dynamic magnetization properties of both the free and reference layers in a CoFeB/MgO p-MTJ subject to in-plane magnetic fields of up to 1.2 T. We compare our experimental results with full micromagnetic simulations of the entire p-MTJ and find excellent agreement for both the static and dynamic behavior of the free and reference layers. The micromagnetic simulations allow us to map out the spatial properties of all the modes as a function of the in-plane field. To reproduce all experimentally observed modes requires a combination of perpendicular and circumferential excitation mechanism, consistent with the combined effect of a voltage dependent PMA and the Oersted field from the microwave current.

II. EXPERIMENT

A. Device fabrication

The stack for the p-MTJ is prepared using dc/rf magnetron sputtering on a sapphire substrate, which consists of Ta(5)/Ru(10)/Ta(5)/$Co_{20}Fe_{60}B_{20}$(0.9)/MgO(1)/$Co_{20}Fe_{60}B_{20}$ (1.6)/Ta(5)/Ru(5) layers, with nominal thicknesses in nm shown in parentheses. Both CoFeB layers are thin enough to have substantial PMA, with the thicker CoFeB considered the free layer due to its smaller PMA value (Fig. 1) [5]. The stack is annealed in vacuum at 300°C for 1 h in a 0.4-T magnetic field perpendicular to the sample plane, which further promotes PMA. The stack is then patterned into a cylindrical pillar with a diameter of 100 nm using electron-beam lithography and argon-ion milling. High-frequency contacts are finally made using evaporation and liftoff.

B. Measurement setup

A schematic of the homodyne-detected FMR setup is shown in Fig. 1. The setup allows for simultaneous measurement of

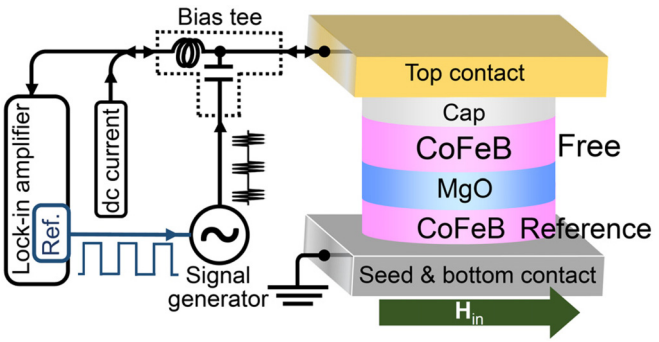

FIG. 1. Schematic of p-MTJ structure and the setup for homodyne-detected FMR measurement.

the resistance R and of the FMR in the in-plane magnetic field H_{in} (resistance measurements under the out-of-plane fields H_{op} are carried out in a different setup). All resistance measurements are, however, carried out with the microwave excitation turned off. FMR measurements with homodyne detection are achieved by passing a pulse-modulated (313 Hz) microwave signal from an rf signal generator to the p-MTJ device via a bias tee [18–21]. At each field value, the microwave frequency f is swept from 3 to 33 GHz, while the microwave power is held constant at -25 dBm. The device response, a dc voltage V_{dc} modulated at 313 Hz, is picked up by the same bias tee and measured in a phase-sensitive manner using a lock-in amplifier, which also provides the 313-Hz reference for the pulse modulation. All measurements are carried out at room temperature.

III. RESULTS

A. Magnetoresistance vs in-plane magnetic field

The resistance R of the p-MTJ device versus the in-plane (hard axis) field H_{in} is shown in Fig. 2(a). The corresponding resistance for the out-of-plane (easy axis) field H_{op} is shown in the inset of the same figure, confirming both the high TMR ratio (76%) and the high-quality single step switching. The R-H_{in} curve shows nonmonotonic behavior with a broad maximum around 0.5 T, which is consistent with the free and reference layers rotating at different rates towards their hard axis on account of their different PMA magnitudes. At low fields, the free- and reference-layer magnetizations are essentially parallel, both aligning with the perpendicular easy axis. As the in-plane field increases, the thicker (lower PMA) free layer deviates more rapidly from the easy axis, leading to an increasing angular separation between the two magnetizations and, as a consequence, an increasing resistance. The resistance then peaks as the free layer approaches saturation, after which the two magnetizations gradually become more parallel. Although the reference layer never fully saturates in-plane for the fields available in our setup, the device resistance almost reaches a fully parallel state at close to 1.2 T.

We can estimate the angle (θ) between the free- and reference-layer magnetizations (θ_F and θ_R) assuming a simple sinusoidal angular dependence of the resistance,

$$R = R_P[(1 - r_{\text{TMR}} \sin^2(\theta/2)(1 + r_{\text{TMR}})]^{-1}, \qquad (1)$$

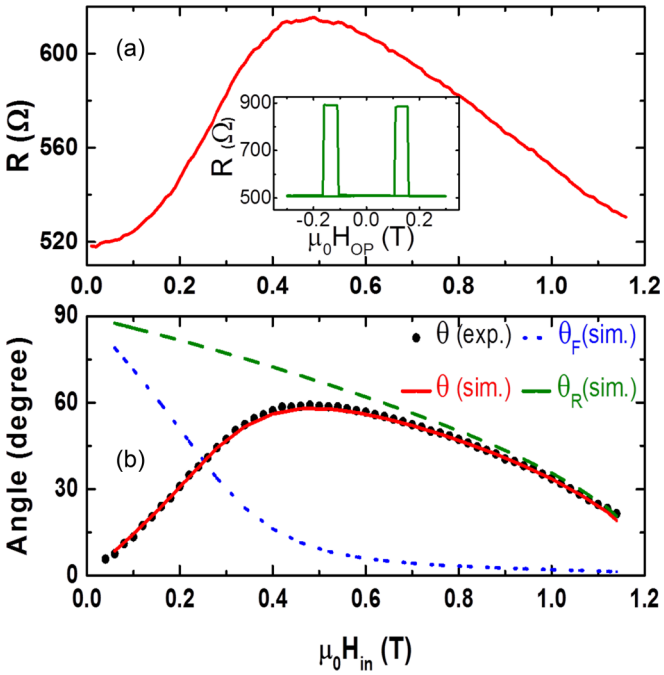

FIG. 2. (a) Junction resistance versus in-plane magnetic field ($R - H_{\text{in}}$). The inset shows the major R-H curve of the perpendicular field H_{op} for the same device. (b) Angle of simulated average magnetization for the free layer (dotted line) and for the reference layer (dashed line). The relative angle of the layers extracted from the simulation (solid line) and calculated from the resistance experiment (filled circles) are in good agreement. μ_0 is permeability.

where R_P is the junction resistance in the parallel state and r_{TMR} is the TMR ratio. The result is shown as the black dots in Fig. 2(b), together with fits based on the micromagnetic simulations described in Sec. IV below.

B. Homodyne-detected FMR vs in-plane magnetic field

Figure 3(a) shows the measured homodyne-detected FMR response vs in-plane field as a contour map of all frequency scans at each magnetic field. The two insets show two examples of FMR spectra (dots) together with fits (solid curves), based on a sum of up to five resonances, where each resonance is allowed to have a symmetric and an antisymmetric Lorentzian lineshape [22],

$$V_{\text{dc}} = \frac{V_S \Delta f^2 + 4V_A(f - f_r)\Delta f}{4(f - f_r)^2 + \Delta f^2} + V_{\text{offset}}, \qquad (2)$$

where f_r is the resonance frequency of the mode, Δf is its linewidth (full width half maximum), V_S and V_A are the coefficients of the symmetrical and antisymmetrical Lorentz functions, respectively, and V_{offset} is the constant offset voltage. The large antisymmetric contribution indicates that the observed FMR is primarily excited by the electric-field modulation of the PMA [15].

At low fields, the observed low-frequency modes first show a substantial softening as the applied field counteracts the PMA. As the in-plane field increases, the mode frequencies reach a minimum well before the maximum relative angle between the two magnetizations. Once the free layer has

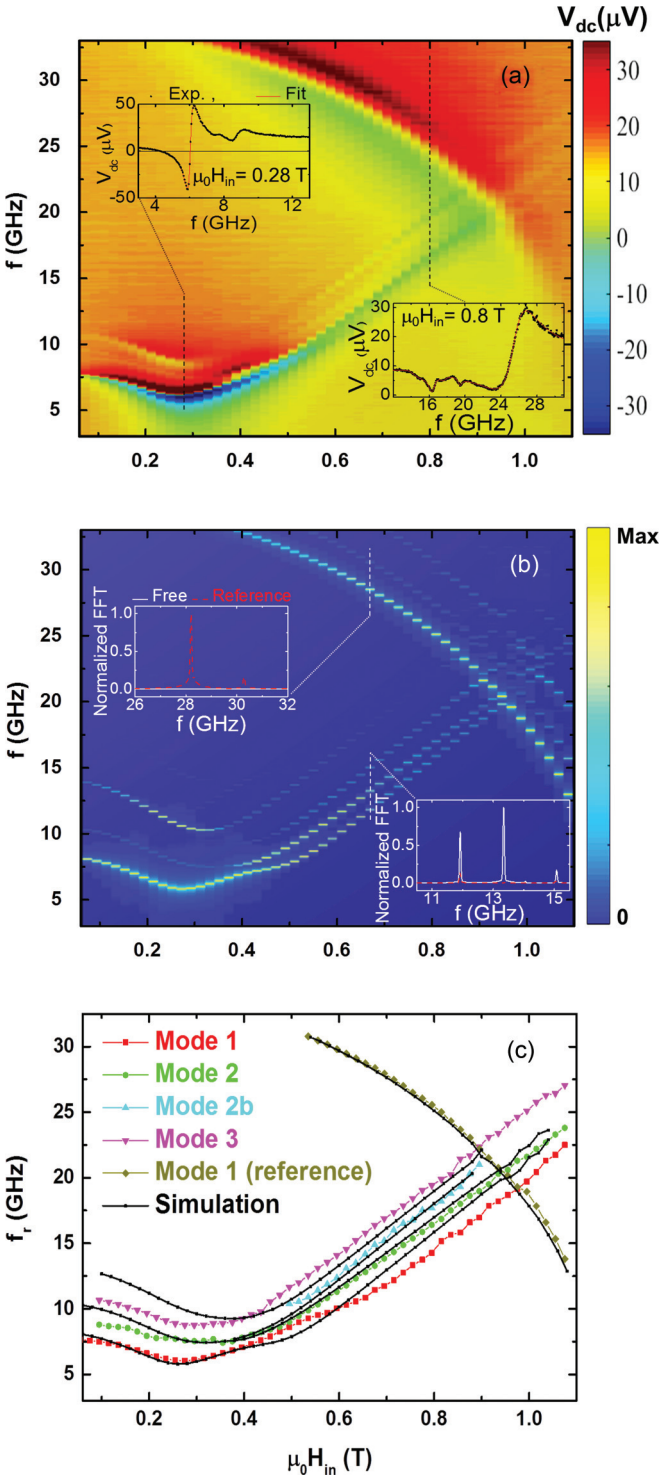

FIG. 3. (a) Homodyne-detected FMR spectra V_{dc} as a function of the in-plane field H_{in} and microwave frequency f. The insets show spectra for selected frequency ranges and field values (dots), and the fitted curves (solid lines) each contain different resonance peaks. (b) FFT spectra extracted from the evolution of the average magnetization of the simulated p-MTJ. Insets represent the contribution of the free layer (solid curves) and reference layer (dashed curves) for each resonance mode. (c) Resonance modes extracted from FMR labeled as modes 1 to 3 for free layer, besides a single mode for reference layer (colorful curves) and modes from micromagnetic simulation (black curves).

saturated in-plane, the frequencies of these modes increase more or less linearly with the applied field.

In addition to these lower frequency modes, a much higher frequency can be observed with a much slower reduction in frequency versus applied field. It is natural to ascribe this much higher frequency to the reference layer, with its much higher in-plane saturation field. As we will show in the next section, this is directly corroborated by micromagnetic simulations.

IV. MICROMAGNETIC SIMULATIONS

A. Fits to the experimental results

A full 3D micromagnetic simulation is carried out to gain further insight into the static and dynamic behavior of the p-MTJ as a function of the applied in-plane magnetic field. The entire p-MTJ is simulated using code from the GPU-based finite-difference micromagnetic package MUMAX3 [23]. The modeled p-MTJ has a circular cross-section, 3.2-nm-thick trilayer pillar, with a 100-nm diameter meshed by a $1.6 \times 1.6 \times 0.8$ nm^3 unit cell size. The free layer and the reference layer are, respectively, 1.6 nm and 0.8 nm thick, and are separated by a 0.8-nm nonmagnetic spacer. We define the x axis as the direction of the in-plane external magnetic field, the y axis as the in-plane direction perpendicular to this, and the z axis as the film normal.

The physical parameters used in the simulation are the saturation magnetization $\mu_0 M_S = 1.5$ T and the exchange stiffness $A_{ex} = 16$ pJ/m for the $Co_{20}Fe_{60}B_{20}$ magnetic layers obtained from previous studies on CoFeB/MgO MTJs [11,24,25]. We ignore any exchange coupling between the magnetic layers mediated through the spacer [10,12,26–30]. We extract the anisotropy constants by tuning them to find the best match between the static measurement and the simulation [shown in Fig. 2(b)], and also between the resonance modes from the FMR measurements and the dynamic micromagnetic simulation. The first- and second-order magnetocrystalline anisotropy constants for the free layer are 1.03×10^6 and 3×10^3 J/m^3, respectively; they are 1.368×10^6 and 2.1×10^4 J/m^3 for the reference layer. A small damping constant $\alpha = 0.0015$, about an order of magnitude smaller than the real value [5], is used to better resolve the different spin-wave peaks in the spectra.

As mentioned above, the large asymmetry of the FMR response indicates that the excitation mechanism is primarily due to electric-field modulation of the PMA [15]. Using a vector network analyzer (VNA), we measure the reflection coefficient of the microwave power and the impedance of the p-MTJ as a function of frequency. Under our experimental conditions, the amplitude of the microwave voltage is then estimated to be about 30 mV, which corresponds to a PMA change of ± 1.6 mT [14]. In addition, we also considered the Oersted field generated by the estimated 70 μA microwave current through the nanopillar (approximated as arising from an infinite cylinder) as this has been shown to drive FMR in the nanocontact geometry [31]. As noted below, it is essential to include the microwave Oersted field in the simulation to reproduce all experimentally observed modes. The excitation field hence has both a PMA component along the z axis and an in-plane, circumferential component. We also include spin-transfer torque (STT) from the microwave current, using a spin polarization factor of 0.5 [32], and a secondary spin-torque

parameter $\epsilon' = 0.2$ [23,33]. Following Ref. [34], we let the time evolution of the excitation field and current follow a sinc field pulse, $\sin(2\pi ft)/(2\pi ft)$, with a cutoff frequency $f = 40$ GHz, which provides equal spectral weight to all frequencies up to the cutoff.

The simulated spin-wave frequencies show very good agreement with the experimentally detected frequencies, as shown in Figs. 3(b) and 3(c), where the power spectral density shown in Fig. 3(b) is obtained from a fast Fourier transform (FFT) of the time-varying y component of the averaged magnetization. The simulated frequencies follow the same trend as the measured frequencies. The layer-resolved analysis of the simulated spin-wave spectrum confirms the attribution of the spin waves to each of the magnetic layers. While the high-frequency peak is confirmed to be excited mainly in the fixed layer, the spin-wave modes at low field and lower frequencies result from free-layer excitation. Their field behavior of softening and subsequently increasing as a function of the field can be explained by the applied field effect counteracting the magnetic anisotropy at low field and increasing the frequency following the in-plane effective field after the in-plane saturation of the free layer. The slight difference between the micromagnetic simulation and measurements could be attributed to the minor differences between the simulated p-MTJ and the actual device. Possible differences include larger thicknesses (spacer and fixed layer are adjusted to fit the discretization of the p-MTJ simulation with a cell thickness of 0.8 nm) as well as the edge roughness (due to discretization in simulation and fabrication variations in the real structure [35]). Such differences can influence both the static [36] and the magnetodynamic properties of the device.

B. Spatial mode profiles

To gain a deeper insight into the excited modes, their simulated spatial profiles are constructed via an FFT for each simulation cell [37] of each magnetic layer in the p-MTJ pillar, as shown in Fig. 4. At low fields, the mode profile can be described as consisting of confined spin-wave modes, conveniently sorted by their radial and azimuthal symmetries. These eigenmodes are dipolar confined spinwave modes and are a consequence of the quantization of the in-plane wave vector due to the finite radius of the pillar [38]. Radial and azimuthal spin waves are described by the integers $[n,m]$, which indicate the number of nodes of the dynamic magnetization components along the radial (n) and azimuthal (m) directions with respect to the disk plane and the center of the magnetic layer of the pillar. Figure 4(a) shows the low-field excited modes, which can be described using Bessel functions [10]. The highest amplitude mode detected experimentally is the free-layer fundamental eigenmode [0,0], in which all the spins precess in-phase with neither the radial nor the azimuthal nodes. Both mode 2 [0,1] and mode 3 [0,2] are azimuthal modes with no radial node. While the electric field driven excitation dominates, the modes with azimuthal nodes are not observed unless the Oersted field excitation is included as they spatially couple to the Oersted field component of the excitation. The simulated mode 4 [1,0] has a radial node and is therefore not detected experimentally due to its lower intensity when averaged over the pillar.

As the in-plane external field strength increases, it gradually overcomes the anisotropy field and rotates the magnetizations towards the disk plane. The fundamental mode has a maximum amplitude around the edge of the p-MTJ pillar, while mode 2 splits into two branches in which the spin waves are localized horizontally and vertically in the disk, as shown in Fig. 4(b), as a result of the broken symmetry of the internal field. By increasing the in-plane field, modes along or orthogonal to the field no longer have the same energy. However, these orthogonal modes are degenerate in the low-field regime where the symmetry of the structure and the field is preserved. The mode frequencies thus depend on their wave vector k and the internal field configuration in the magnetic disk layer [39,40].

In the high-field regime, all free-layer modes suffer from increasing localization around the edges of the magnetic disk layer due to the increase in the inhomogeneity of the

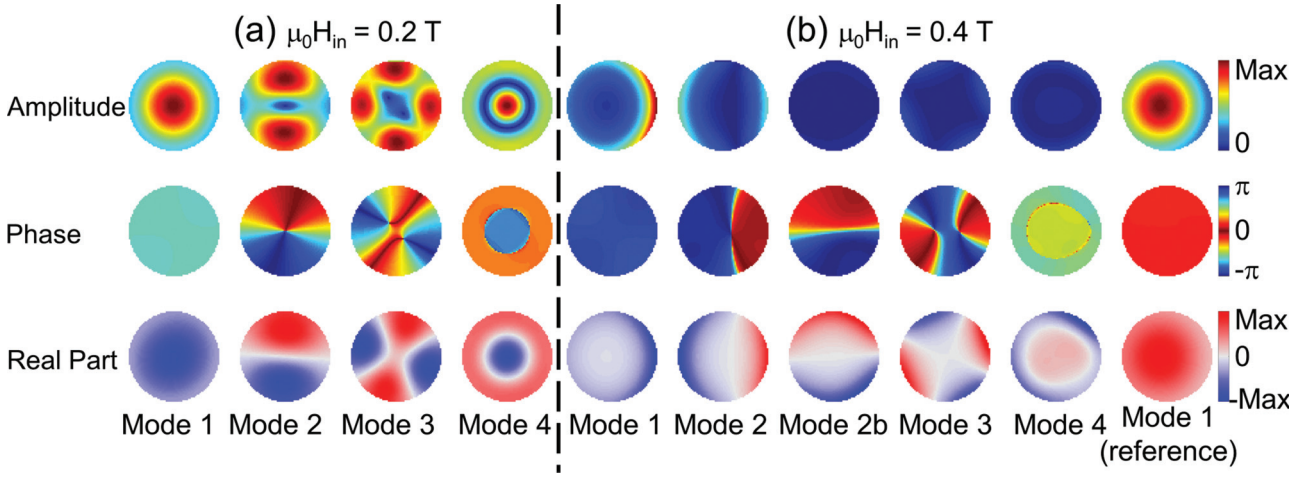

FIG. 4. (a) Spatial profile of amplitude (upper row), phase (middle row), and real part (lower row) for the first four free-layer modes at $\mu_0 H_{in}$=0.2 T. (b) Spatial profile of the modes at $\mu_0 H_{in}$=0.4 T where mode 2 starts to split and mode 1 to be localized at the edge. All modes are from the free layer except the mode labeled mode 1 (reference), which is the fundamental mode of the reference layer.

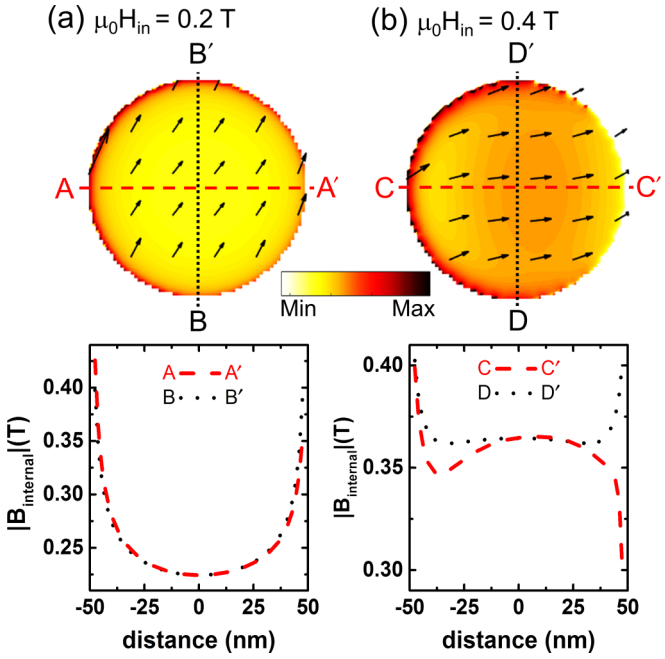

FIG. 5. Internal field spatial profile for (a) low-field regime ($\mu_0 H_{in}$=0.2 T); this is minimum in the center of the disk with cylindrical symmetry. (b) High-field regime ($\mu_0 H_{in}$=0.4 T) with broken symmetry and inhomogeneity; minimum value at right side edge. While the color map shows the amplitude of the internal field, the vertical and horizontal directions for the arrows show its components in the z direction and x directions, respectively.

internal field in the disk. Localization of the modes happens at sites where the internal field is more homogeneous and at a minimum [41]; as the internal field varies in the disk, spins can no longer resonate at the same frequency. Thus, in addition to the wave vector k, the internal field plays a significant role in the confinement and localization of the modes in the disk layer. As shown for mode 1 at low fields, maximum resonance amplitude occurs in the center of the disk where the internal field is more homogeneous and minimum [Fig. 4(a)]. By increasing the applied field strength, the maximum amplitude for this mode occurs in a ring-shaped region near the edges of the disk at intermediate field values (not shown here), and in the high-field regime, this mode becomes localized near the right-hand side of the disk [Fig. 4(b)], where the internal field is at a minimum. Figure 5 shows the internal field amplitude for the free layer for low (a) and high fields (b). Meanwhile in the low-field regime, cylindrical symmetry is mostly conserved and the internal field is homogeneous in the center of the disk with minimum amplitude. In the high-field regime, the cylindrical symmetry of the magnetic free disk layer is broken, and the internal field is almost aligned with the external field, having a minimum at the sides along the direction of the applied field, due to the stray fields from the magnetic poles in these regions [Fig. 5(b)].

The fundamental mode of the reference layer, labeled Mode 1 (reference), is also a radial mode [0,0], and is shown in Fig. 4(b). As the magnetic anisotropy field in the reference layer is much stronger than the free-layer anisotropy, this mode is excited at higher frequencies and its symmetry survives to higher field.

V. CONCLUSIONS

We have presented the static and dynamic magnetization properties of an all-perpendicular magnetic tunnel junction (p-MTJ) pillar in an in-plane magnetic field. By combining experimental measurements of magnetoresistance and homodyne-detected ferromagnetic resonance (FMR) spectroscopy with micromagnetic numerical simulation, we were able to show the static configuration and the observed resonance peaks due to dynamic excitation of each of the magnetic layers of the p-MTJ. We identified the excited modes as dipolar confined modes with radial and azimuthal symmetry on account of the quantization of the wave vector that results from geometrical confinement; their evolution with the applied field was understood as a result of the distribution of the internal magnetic field reflected in the localization of the modes around the edges of the disk layer where the effective field is minimum and homogeneous. We finally conclude that the excitation mechanism is a combination of the microwave voltage modulated perpendicular magnetic anisotropy, the microwave Oersted field, and the spin-transfer torque generated by the microwave current.

ACKNOWLEDGMENTS

We gratefully acknowledge A. Eklund and G. Malm for the VNA measurements. Support from the Swedish Foundation for Strategic Research (SSF), the Swedish Research Council (VR), the Knut and Alice Wallenberg Foundation, and the ERC through the Starting Grant 307144 “Mustang,” is gratefully acknowledged. The work at Tohoku University was supported in part by an R&D Project for ICT Key Technology of MEXT, a Grant-in-Aid for Scientific Research from MEXT (Grant No. 26103002), and Cooperative Research Project of RIEC, Tohoku University.

[1] W. H. Butler, X.-G. Zhang, T. C. Schulthess, and J. M. MacLaren, Phys. Rev. B **63**, 054416 (2001).
[2] S. S. P. Parkin, C. Kaiser, A. Panchula, P. M. Rice, B. Hughes, M. Samant, and S.-H. Yang, Nat. Mater. **3**, 862 (2004).
[3] S. Yuasa, T. Nagahama, A. Fukushima, Y. Suzuki, and K. Ando, Nat. Mater. **3**, 868 (2004).
[4] S. Ikeda, J. Hayakawa, Y. Ashizawa, Y. M. Lee, K. Miura, H. Hasegawa, M. Tsunoda, F. Matsukura, and H. Ohno, Appl. Phys. Lett. **93**, 082508 (2008).
[5] S. Ikeda, K. Miura, H. Yamamoto, K. Mizunuma, H. D. Gan, M. Endo, S. Kanai, J. Hayakawa, F. Matsukura, and H. Ohno, Nat. Mater. **9**, 721 (2010).

[6] H. Gan, R. Malmhall, Z. Wang, B. K. Yen, J. Zhang, X. Wang, Y. Zhou, X. Hao, D. Jung, K. Satoh, and Y. Huai, Appl. Phys. Lett. **105**, 192403 (2014).
[7] Q. L. Ma, X. M. Zhang, T. Miyazaki, and S. Mizukami, AIP Adv. **5**, 087177 (2015).
[8] Z. Kugler, J.-P. Grote, V. Drewello, O. Schebaum, G. Reiss, and A. Thomas, J. Appl. Phys. **111**, 07C703 (2012).
[9] T. Chen, R. K. Dumas, A. Eklund, P. K. Muduli, A. Houshang, A. A. Awad, P. Dürrenfeld, B. G. Malm, A. Rusu, and J. Åkerman, Proc. IEEE **104**, 1919 (2016).
[10] V. V. Naletov, G. de Loubens, G. Albuquerque, S. Borlenghi, V. Cros, G. Faini, J. Grollier, H. Hurdequint, N. Locatelli, B. Pigeau, A. N. Slavin, V. S. Tiberkevich, C. Ulysse, T. Valet, and O. Klein, Phys. Rev. B **84**, 224423 (2011).
[11] K. Mizunuma, M. Yamanouchi, H. Sato, S. Ikeda, S. Kanai, F. Matsukura, and H. Ohno, Appl. Phys. Express **6**, 063002 (2013).
[12] E. Hirayama, S. Kanai, H. Sato, F. Matsukura, and H. Ohno, J. Appl. Phys. **117**, 17B708 (2015).
[13] E. Hirayama, S. Kanai, K. Sato, M. Yamanouchi, H. Sato, S. Ikeda, F. Matsukura, and H. Ohno, Jpn. J. Appl. Phys. **54**, 04DM03 (2015).
[14] E. Hirayama, S. Kanai, J. Ohe, H. Sato, F. Matsukura, and H. Ohno, Appl. Phys. Lett. **107**, 132404 (2015).
[15] T. Nozaki, Y. Shiota, S. Miwa, S. Murakami, F. Bonell, S. Ishibashi, H. Kubota, K. Yakushiji, T. Saruya, A. Fukushima, S. Yuasa, T. Shinjo, and Y. Suzuki, Nat. Phys. **8**, 491 (2012).
[16] D. Tiwari, N. Sisodia, R. Sharma, P. Dürrenfeld, J. Åkerman, and P. K. Muduli, Appl. Phys. Lett. **108**, 082402 (2016).
[17] J. Zhu, J. A. Katine, G. E. Rowlands, Y.-J. Chen, Z. Duan, J. G. Alzate, P. Upadhyaya, J. Langer, P. K. Amiri, K. L. Wang, and I. N. Krivorotov, Phys. Rev. Lett. **108**, 197203 (2012).
[18] J. C. Sankey, P. M. Braganca, A. G. F. Garcia, I. N. Krivorotov, R. A. Buhrman, and D. C. Ralph, Phys. Rev. Lett. **96**, 227601 (2006).
[19] J. C. Sankey, Y.-T. Cui, J. Z. Sun, J. C. Slonczewski, R. A. Buhrman, and D. C. Ralph, Nat. Phys. **4**, 67 (2007).
[20] W. Chen, G. de Loubens, J.-M. L. Beaujour, J. Z. Sun, and A. D. Kent, Appl. Phys. Lett. **95**, 172513 (2009).
[21] X. Cheng, J. A. Katine, G. E. Rowlands, and I. N. Krivorotov, Appl. Phys. Lett. **103**, 082402 (2013).
[22] L. Liu, T. Moriyama, D. C. Ralph, and R. A. Buhrman, Phys. Rev. Lett. **106**, 036601 (2011).
[23] A. Vansteenkiste, J. Leliaert, M. Dvornik, M. Helsen, F. Garcia-Sanchez, and B. Van Waeyenberge, AIP Advances **4**, 107133 (2014).
[24] H. Sato, M. Yamanouchi, K. Miura, S. Ikeda, F. Matsukura, and H. Ohno, IEEE Magn. Lett. **3**, 3000204 (2012).
[25] M. Yamanouchi, A. Jander, P. Dhagat, S. Ikeda, F. Matsukura, and H. Ohno, IEEE Magn. Lett. **2**, 3000304 (2011).
[26] J. Faure-Vincent, C. Tiusan, C. Bellouard, E. Popova, M. Hehn, F. Montaigne, and A. Schuhl, Phys. Rev. Lett. **89**, 107206 (2002).
[27] H.-C. Wu, S. K. Arora, O. N. Mryasov, and I. V. Shvets, Appl. Phys. Lett. **92**, 182502 (2008).
[28] H. Yanagihara, Y. Toyoda, and E. Kita, J. Appl. Phys. **101**, 09D101 (2007).
[29] A. A. Awad, A. Lara, V. Metlushko, K. Y. Guslienko, and F. G. Aliev, Appl. Phys. Lett. **100**, 262406 (2012).
[30] T. Katayama, S. Yuasa, J. Velev, M. Y. Zhuravlev, S. S. Jaswal, and E. Y. Tsymbal, Appl. Phys. Lett. **89**, 112503 (2006).
[31] M. Fazlali, M. Dvornik, E. Iacocca, P. Dürrenfeld, M. Haidar, J. Åkerman, and R. K. Dumas, Phys. Rev. B **93**, 134427 (2016).
[32] M. Julliere, Phys. Lett. A **54**, 225 (1975).
[33] D. E. Nikonov, G. I. Bourianoff, G. Rowlands, and I. N. Krivorotov, J. Appl. Phys. **107**, 113910 (2010).
[34] K. S. Lee, D. S. Han, and S. K. Kim, Phys. Rev. Lett. **102**, 127202 (2009).
[35] K. Kinoshita, H. Honjo, S. Fukami, H. Sato, K. Mizunuma, K. Tokutome, M. Murahata, S. Ikeda, S. Miura, N. Kasai, and H. Ohno, Jpn. J. Appl. Phys. **53**, 103001 (2014).
[36] C. A. F. Vaz, C. Athanasiou, J. A. C. Bland, and G. Rowlands, Phys. Rev. B **73**, 054411 (2006).
[37] R. D. McMichael and M. D. Stiles, J. Appl. Phys. **97**, 10J901 (2005).
[38] G. N. Kakazei, P. E. Wigen, K. Y. Guslienko, V. Novosad, A. N. Slavin, V. O. Golub, N. A. Lesnik, and Y. Otani, Appl. Phys. Lett. **85**, 443 (2004).
[39] M. Buess, R. Höllinger, T. Haug, K. Perzlmaier, U. Krey, D. Pescia, M. R. Scheinfein, D. Weiss, and C. H. Back, Phys. Rev. Lett. **93**, 077207 (2004).
[40] J. P. Park and P. A. Crowell, Phys. Rev. Lett. **95**, 167201 (2005).
[41] F. Giesen, J. Podbielski, and D. Grundler, Phys. Rev. B **76**, 014431 (2007).